Journal of Alloys and Compounds 1025 (2025) 180214

Contents lists available at ScienceDirect

Journal of Alloys and Compounds

journal homepage: www.elsevier.com/locate/jalcom

In-situ monitoring the structural pathway of a Ti-based alloy from metallic liquid to metallic glass

Konstantinos Georgarakis [a,*], Martin E. Stiehler [a,*], Louis Hennet [b], Yaofeng Guo [c], Jerzy Antonowicz [d], Dmitri V. Louzguine-Luzgin [e,f], Mark R. Jolly [a], Jérôme Andrieux [g], Gavin B.M. Vaughan [h], A. Lindsay Greer [i]

[a] Faculty of Engineering and Applied Sciences, Cranfield University, MK43 0AL, UK
[b] ICMN – UMR 7374 CNRS et Université d'Orléans, Orléans 45071, France
[c] Protochips, Inc., Morrisville, NC 27560, USA
[d] Faculty of Physics, Warsaw University of Technology, Warsaw, Poland
[e] Advanced Institute for Materials Research (WPI-AIMR), Tohoku University, Sendai 980-8577, Japan
[f] MathAM-OIL, National Institute of Advanced Industrial Science and Technology (AIST), Sendai 980-8577, Japan
[g] Université Claude Bernard Lyon 1, CNRS, LMI UMR 5615, Villeurbanne 69100, France
[h] European Synchrotron Radiation Facility, Grenoble 38042, France
[i] Department of Materials Science & Metallurgy, University of Cambridge, CB3 0FS, UK

ARTICLE INFO

Keywords:
Metallic glasses
Vitrification
Atomic structure
Levitation
Synchrotron radiation
Structure formation

ABSTRACT

A metallic glass is formed when a molten metallic alloy is cooled rapidly enough that crystallisation is avoided. However, the way the atomic structure of the liquid converts to that of the glass is generally unknown. The main challenge is the sufficiently fast experimental acquisition of structural data in the undercooled liquid regime necessitated by the high cooling rates needed to avoid crystallisation. In the present study, using aerodynamic levitation, the Ni-free Ti-based alloy $Ti_{40}Zr_{10}Cu_{34}Pd_{14}Sn_2$ was vitrified in-situ in a high-energy synchrotron X-ray beam while diffraction data were acquired during cooling from above the liquidus temperature T_{liq} to well below the glass-transition temperature T_g. The structure in the undercooled liquid regime shows an accelerated evolution. Both the local order in the short (SRO) and medium range (MRO) increases rapidly as the undercooled liquid approaches T_g, below which the amorphous structure "freezes". Nevertheless, distinct differences between the evolution of SRO and MRO were observed. The structural rearrangements in the undercooled liquid are found to be correlated with a rapid increase in viscosity of the metallic liquid upon cooling. The new findings shed light on the evolution of the atomic structure of metallic liquids during vitrification and the structural origins of the sluggish kinetics that suppress nucleation and growth of crystalline phases.

1. Introduction

Understanding the remarkable kinetic arrest in glass-forming liquids and the dramatic change in viscosity by more than 12 orders of magnitude between liquidus temperature T_{liq} and glass-transition temperature T_g is one of the most intriguing unresolved issues in materials research. Although the underlying microscopic origins remain unclear, recent studies indicate a relation with the evolution of the atomic structure of the glass-forming liquids [1–5]. Depending on the evolution of viscosity as a function of temperature, liquids can be categorised into strong and fragile [6]. Strong liquids exhibit Arrhenius-type behaviour which implies a simple thermally activated behaviour for viscosity $\eta(T) = \eta_o \exp(E_A/k_B T)$ where T is the temperature, η_o a pre-exponential factor related to the viscosity at infinite temperature, k_B the Boltzmann constant and E_A an effective activation energy for viscous flow. The viscosity of a fragile liquid, however, markedly departs from this function and exhibits non-Arrhenius behaviour. The bigger the deviation from Arrhenius behaviour the more fragile the liquid is, with viscosity increasing rapidly as T_g is approached [7]. The fragility of metallic liquids is usually high. Due to their relatively simple structure, as compared to polymers and oxides, investigation of metallic undercooled liquids offers unique opportunities for improving our understanding of glass

* Corresponding authors.
E-mail addresses: k.georgarakis@cranfield.ac.uk (K. Georgarakis), martin.stiehler@cranfield.ac.uk (M.E. Stiehler).

https://doi.org/10.1016/j.jallcom.2025.180214
Received 22 January 2025; Received in revised form 1 April 2025; Accepted 2 April 2025
Available online 3 April 2025

formation and glass transition. Recent advances in containerless solidification methods such as electrostatic and aerodynamic levitation provide new possibilities to study the structure of undercooled metallic liquids using synchrotron and neutron scattering techniques [8,9]. Nevertheless, the acquisition of structural information in the whole temperature range from the liquid to the glassy state for metallic liquids remains challenging since avoiding crystallisation during quenching requires cooling rates that are not easily achievable in in-situ diffraction experiments. Related results not only contribute considerably to the basic understanding of these materials but also of their application-related aspects. Metallic glasses offer an attractive combination of engineering properties such as high mechanical strength, high elastic strain, good corrosion resistance and excellent soft magnetic properties [10–13]. Furthermore, compared to their crystalline counterparts, metallic glasses exhibit lower Young's, bulk and shear moduli reduced by about 10 %, 6 % and 30 %, respectively [11]. These characteristics make them attractive for a variety of applications including biomedical body implants, potentially diminishing the stress shielding effect that is often associated with conventional metallic implants [14]. However, many of the bulk-glass-forming alloys contain toxic elements such as Be, Ni, V or Al [14,15]. In this respect, Ti-based metallic glasses, free of toxic elements, are a particularly interesting class of alloys with high specific strength and good biocompatibility [13,14,16,17–19]. Among the Ni-free Ti-based metallic glasses, $Ti_{40}Zr_{10}Cu_{34}Pd_{14}Sn_2$ possesses the highest glass-forming ability (GFA) with a critical diameter d_c bigger than 10 mm [20]. Recent in-situ high-energy synchrotron diffraction experiments yielded results on the structural evolution of $Ti_{40}Zr_{10}Cu_{34}Pd_{14}Sn_2$ metallic glass upon heating from room-temperature towards crystallisation including signs of a possible metallic glacial glass phase [21–24]. Revealing the structural evolution during vitrification may offer new insights into the glass formation in Ti-based alloys supporting the design of biocompatible alloys with high bulk GFA and high functionality.

In the present work, aerodynamic levitation was used for in-situ probing the structure of the $Ti_{40}Zr_{10}Cu_{34}Pd_{14}Sn_2$ bulk-glass-forming alloy continuously along its pathway from equilibrium to undercooled liquid and through vitrification in a high-energy, high-flux synchrotron beam. The results indicate an accelerated structural evolution of the short (SRO) and medium range order (MRO) in the undercooled liquid towards T_g.

2. Materials and methods

Spherical ingots, about 2 mm in diameter, of a quinary alloy with the nominal composition $Ti_{40}Zr_{10}Cu_{34}Pd_{14}Sn_2$ (in at%) were prepared by arc melting from high-purity raw materials (Ti: 99.9 %, Zr: 99.8 %, Cu: 99 %, Pd: 99 %, Sn: 99.8 %) under Ar atmosphere. Remelting five times ensured chemical homogeneity. A sphere of the alloy was then levitated by high-purity Ar flow through an Al nozzle [8] and melted using two CO_2-laser beams. During the subsequent free cooling the alloy's structure was investigated in-situ by high-energy X-ray diffraction in transmission mode carried out at beamline ID15 of the European Synchrotron Radiation Facility (ESRF) in the temperature range between 1473 K (well above T_{liq} = 1176 K (Table 1)) and 487 K (well below the calorimetric glass transition temperature T_g = 689 K (Table 1)). The wavelength of the incident monochromatic beam was $\lambda_i = 0.1245$ Å (E_i = 100 keV). X-ray diffraction patterns were continuously recorded by a Perkin-Elmer two-dimensional flat-panel detector with a time resolution of 100 ms as function of the scattering vector $\vec{Q}$ (with modulus $Q = \left|\vec{Q}\right|$ up to 25 Å^{-1}), where $Q = 4\pi \sin\theta / \lambda$ and 2θ the diffraction angle. Two optical pyrometers working at 1.625 μm (623 K - 2073 K) and 0.9 μm (1173 K - 3573 K), respectively, were used to measure the temperature T. Values below 623 K were calculated assuming a continued exponential temperature drop (Fig. 1). The average cooling rate during vitrification was of the order of 80 K/s with an initial cooling rate of the order of 150 K/s. The temperature calibration was verified using T_m and the crystallisation temperature T_X of the alloy (Table 1). The accuracy of the temperature values was estimated to be around ± 12 K above 900 K and better than ± 7 K below 900 K. The high cooling rates that can be achieved in our setup sets the experiment apart from similar studies using other containerless levitation techniques like electromagnetic [27] or electrostatic levitation [9]. This allows for the in-situ vitrification of metallic melts, like $Ti_{40}Zr_{10}Cu_{34}Pd_{14}Sn_2$, that have a comparatively low GFA. Minor non-amorphous features of unknown origin have been observed in a limited number of patterns below $T \approx 950$ K which were exempted from further analysis.

For each temperature T the diffraction images were azimuthally integrated after corrections for polarisation and dark currents using the FIT2D software [28] yielding the integrated diffraction intensities $I(Q, T)$. After corrections for sample absorption, fluorescence, Compton scattering, Laue diffuse scattering, background contribution and normalisation to the atomic X-ray form factor the total structure factors $S(Q, T)$ were obtained with the help of the PDFgetX3 software package [29]. For structural analysis in real space PDFgetX3 furthermore performs the Fourier transformation [30] of $S(Q, T)$ yielding the reduced pair distribution function

$$G(r,T) = \frac{2}{\pi} \int_0^{Q_{max}} Q[S(Q,T) - 1]\sin(Qr)\mathrm{d}Q \quad , \tag{1}$$

with an upper integration limit of $Q_{max} = 15$ Å^{-1} in the present case.

3. Results

Fig. 1 shows the temperature-time dependence $T(t)$ of the $Ti_{40}Zr_{10}Cu_{34}Pd_{14}Sn_2$ sample during cooling. The absence of recalescence indicates that crystallisation was avoided during solidification leading to the formation of a metallic glass.

Table 1
Thermophysical parameters of $Ti_{40}Zr_{10}Cu_{34}Pd_{14}Sn_2$ acquired by calorimetric methods taken from literature (the undercooled-liquid range $\Delta T_X = T_X - T_g$, the reduced glass-transition temperature $T_{rg} = T_g / T_{liq}$ as well as all average values were calculated here).

T_g [K]	T_X [K]	T_m [K]	T_{liq} [K]	ΔT_X [K]	T_{rg}	Ref.
689	739	1126	1187	50	0.58	[20]
682	740	—	1164	58	0.59	[25]
695	743	—	—	48	—	[21]
688	730	—	—	42	—	[26]
689	738	1126	1176	50	0.59	average

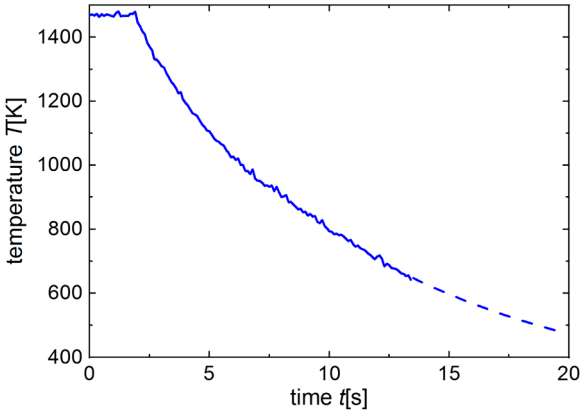

Fig. 1. Temperature-time dependence $T(t)$ of the $Ti_{40}Zr_{10}Cu_{34}Pd_{14}Sn_2$ sample during free cooling in the aerodynamic levitation setup while in the synchrotron beam (the temperatures below 620 K (dashed) were calculated assuming exponential behaviour).

Fig. 2 shows a set of X-ray diffraction results in the form of the structure factor $S(Q, T)$ recorded along the complete pathway. The observed change of the $S(Q, T)$ with decreasing temperature indicates structural evolution that leads to a more ordered structure during cooling. In particular, the shift of the maximum $Q_1(T)$ of the first peak, corresponding to the first diffuse diffraction halo, to higher Q with decreasing temperature T is consistent with the macroscopic volume contraction during cooling [31]. In addition, the increase of $S(Q_1(T), T)$ and the splitting of the second peak, corresponding to second diffuse diffraction halo, centred at around 5.2 $Å^{-1}$ observed during cooling clearly indicate an increasingly ordered structure at lower temperatures. This splitting is a frequent observation in metallic glasses and was discussed in relation to characteristic distances of the SRO [32]. It is interesting to note that it is mainly the low-Q feature of the second halo that is changing during cooling while the shoulder at the high-Q side remains almost unchanged over the complete measured T-range indicating that the responsible structure is already present at high T in the equilibrium liquid (Fig. 2). For a better visualisation of the structural changes in reciprocal space the reader is referred to Movie 1 of the Supplementary Material.

Supplementary material related to this article can be found online at doi:10.1016/j.jallcom.2025.180214.

In order to follow the structural evolution during cooling, several structural metrics derived from the first peak in $S(Q, T)$ over the complete T-range studied were analysed (Fig. 3). Fig. 3a shows the position $Q_{1,cent}(T)$ of the centroid of the peak (black circles). Centroids are also used for the analysis of other peaks throughout this study since they are comparatively less noisy as their calculation involves an integration over a complete peak which provides the opportunity to treat split peaks as well as non-split peaks in the same way without the need for background subtraction or assumption of a specific fit function. Furthermore, the height $S(Q_1(T), T)$ (Fig. 3b) and the full width at half maximum (FWHM) $\Delta Q_1(T)$ (Fig. 3c) are shown. The quantities are directly derived from the experimental data (grey shaded area in the inset of Fig. 3a) without any fitting [3,33]. Especially $Q_{1,cent}(T)$ and $S(Q_1(T), T)$ show non-linear behaviour. This indicates an accelerated structural ordering similar to what has been previously observed for $Zr_{60}Cu_{30}Al_{10}$ [3] and $Zr_{55}Cu_{30}Ni_5Al_{10}$ [2]. Also similar to $Zr_{60}Cu_{30}Al_{10}$, a clear kink occurs near the calorimetric glass-transition temperature T_g for almost all structural metrics presented (vertical dashed line in Fig. 3). Below, the metrics show linear behaviour (Fig. 3).

Supplementary material related to this article can be found online at doi:10.1016/j.jallcom.2025.180214.

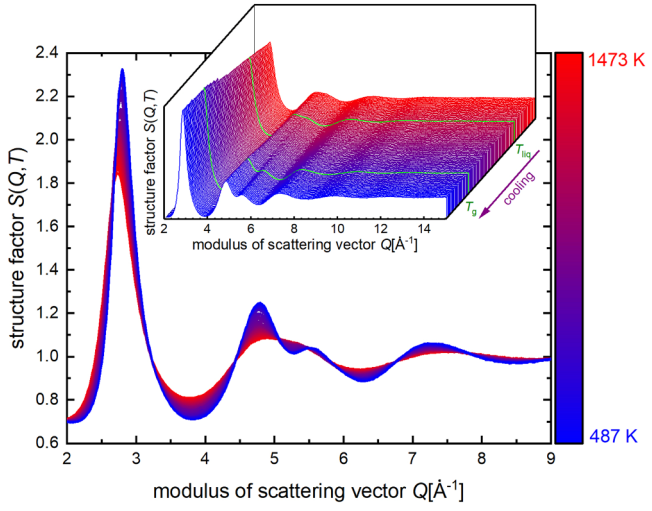

Fig. 2. The evolution of the structure factor $S(Q, T)$ of $Ti_{40}Zr_{10}Cu_{34}Pd_{14}Sn_2$ during free cooling from 1473 K to 487 K; the inset shows a three-dimensional representation of the same data. See also Supplementary Movie 1.

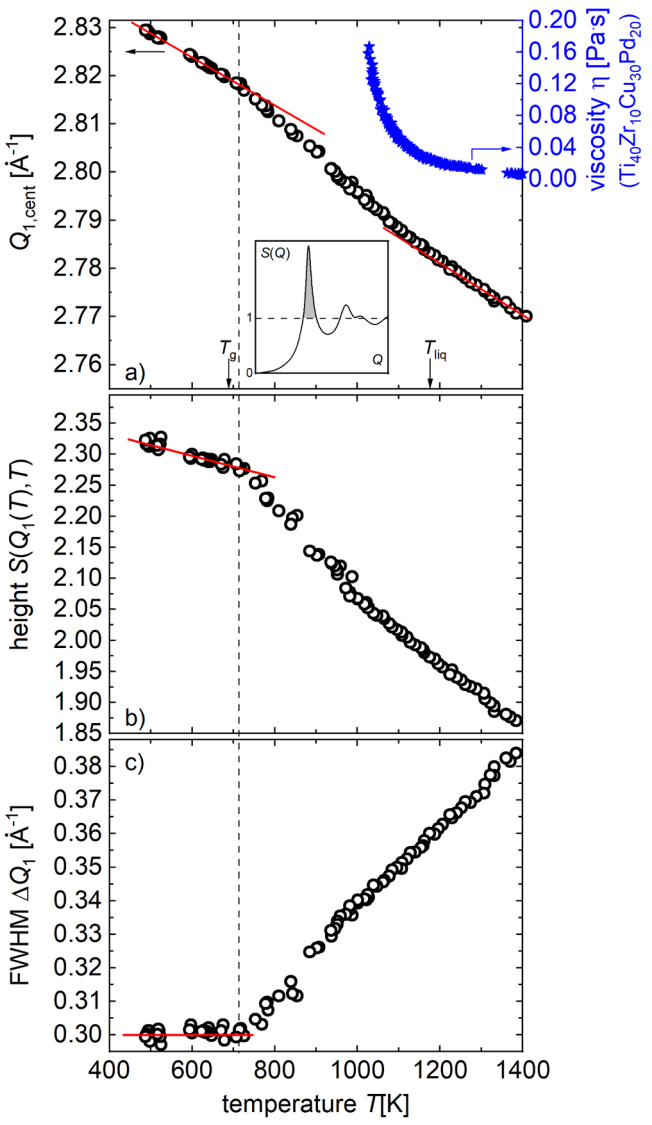

Fig. 3. Structural metrics of $Ti_{40}Zr_{10}Cu_{34}Pd_{14}Sn_2$ in reciprocal space during free cooling derived from the first peak (relevant portion shaded in grey in the inset) of the structure factor $S(Q, T)$. a) position of the centroid $Q_{1,cent}(T)$ (black circles) as well as the viscosity $\eta(T)$ of $Ti_{40}Zr_{10}Cu_{30}Pd_{20}$ (T_g = 687 K [16], T_{liq} = 1279 K [34] replotted from Mauro et al. [4]) (blue stars), b) the height $S(Q_1(T), T)$ and c) the FWHM $\Delta Q_1(T)$. The vertical dashed line indicates the temperature where an abrupt change in the behaviour of the metrics occurs. All other lines are guides for the eye. The arrows in a) indicate the average values of the thermophysically obtained T_g and T_{liq} of $Ti_{40}Zr_{10}Cu_{34}Pd_{14}Sn_2$ given in Table 1.

The reduced pair distribution function $G(r, T)$ (Fig. 4a and Supplementary Movie 2) evolves noticeably with decreasing T, reflecting the changes towards vitrification as well. The first peak of $G(r, T)$, corresponding to the first nearest-neighbour shell, changes only very slightly in position, but increases in intensity and decreases in width indicating a narrower distribution of interatomic distances as well as a gradual increase in the number of atoms in the first shell. For the remainder of this paper, as adopted from [33], the term shell is used for regions with $G(r, T) > 0$ (hatched in green in inset of Fig. 4). The shells are numbered consecutively (n = 1, 2, 3, …) with increasing distance from the central atom at r = 0 Å. The regions with $G(r, T) < 0$ are denoted as anti-shells (cross-hatched in orange in inset of Fig. 4) [33].

The second shell also evolves and a shoulder gradually develops on the high-r side ($r_{2h} \approx 5.4$ Å) resulting in a partial splitting of the peak at lower temperatures. A split second shell is considered a characteristic

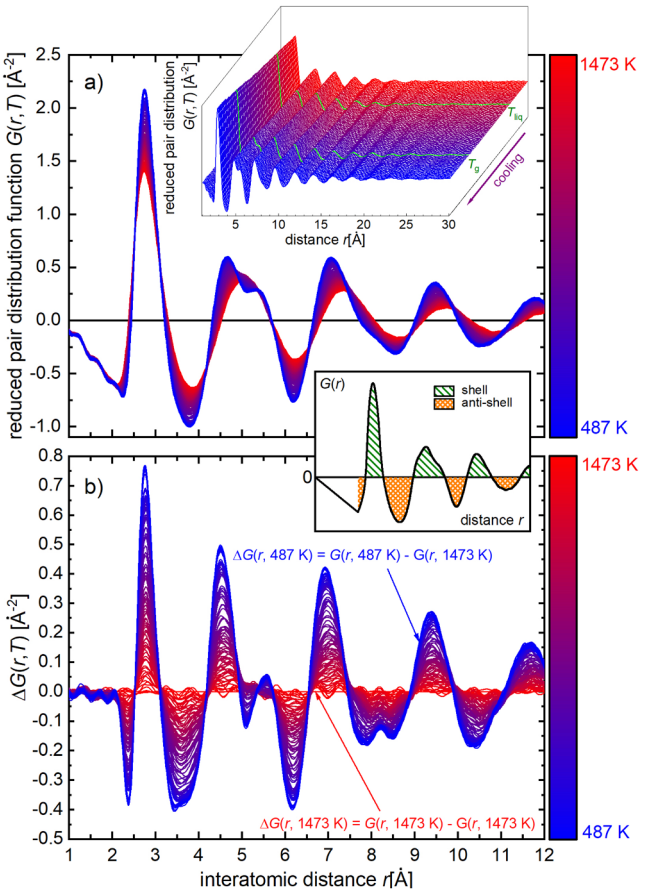

Fig. 4. a) The evolution of the reduced pair distribution function $G(r, T)$ during cooling from 1473 K to 487 K (cf. also Supplementary Movie 2); the inset shows a three-dimensional representation of the same data. b) $\Delta G(r, T) = G(r, T) - G(r, 1473\ \mathrm{K})$ functions showing the increasing difference between $G(r, T)$ at various temperatures during cooling and the one at 1473 K. Inset: $G(r, 478\ \mathrm{K})$ to recall the shell/anti-shell concept [33] (see text).

difference between the glassy and the liquid state attributed to the enhancement of chemical and topological MRO [35]. The shells with $n \geq 3$ shift to smaller interatomic distances r and increase in height during cooling. The presence of clearly distinguishable shells in $G(r, T)$ extends up to about $r \approx 18$ Å at higher temperatures (liquid state), whereas at lower temperatures (glassy state) shells can clearly be observed up to $r \approx 25$ Å (cf. three-dimensional representation in Fig. 4a), indicating an extension of the MRO along the pathway from the liquid to the glassy state. This is consistent with an increasing coherence length $2\pi/\Delta Q_1(T)$ (c.f. decreasing FWHM $\Delta Q_1(T)$ during cooling in Fig. 3c). It is important to note that, in addition to the increasing height of $G(r, T)$ at the shells, the local minima of $G(r, T)$ (anti-shells) become more pronounced as well during cooling, indicating a migration of atoms from anti-shells to shells. This migration has been linked to the cluster evolution during glass formation leading to a distinct increase of the local ordering [3].

The visibility of the evolution of $G(r, T)$ can be enhanced by calculating $\Delta G(r, T) = G(r, T) - G(r, 1473\ \mathrm{K})$ highlighting the changes in $G(r, T)$ compared to that of the highest measured temperature (Fig. 4b). The local maxima of $\Delta G(r, T)$ correspond to the increase of atomic population in the shells, whereas negative $\Delta G(r, T)$ correspond to the decrease of the number of atoms in the anti-shells. Especially the visibility of the increasingly split second shell in $G(r, T)$ (Fig. 4a) that develops during cooling is underlined by the two maxima at $r \approx 4.5$ Å and $r \approx 5.5$ Å in $\Delta G(r, T)$ (Fig. 4b). Furthermore, $\Delta G(r, T)$ emphasises that the evolution of $G(r, T)$ with decreasing T extends up to high r, indicating a significant enhancement of SRO as well as MRO along the alloy's pathway to vitrification. Integrating $\Delta G(r, T)$ for $\Delta G(r, T) > 0$ (purple region in inset of Fig. 5d) yields the same value for each T (purple dots in Fig. 5d) as the absolute values of the integral of $\Delta G(r, T)$ for $\Delta G(r, T) < 0$ (green region in inset of Fig. 5d and green dots in Fig. 5d). This not only corroborates the mentioned migration but also indicates the continuous acceleration of this effect during cooling, supporting the observations in reciprocal

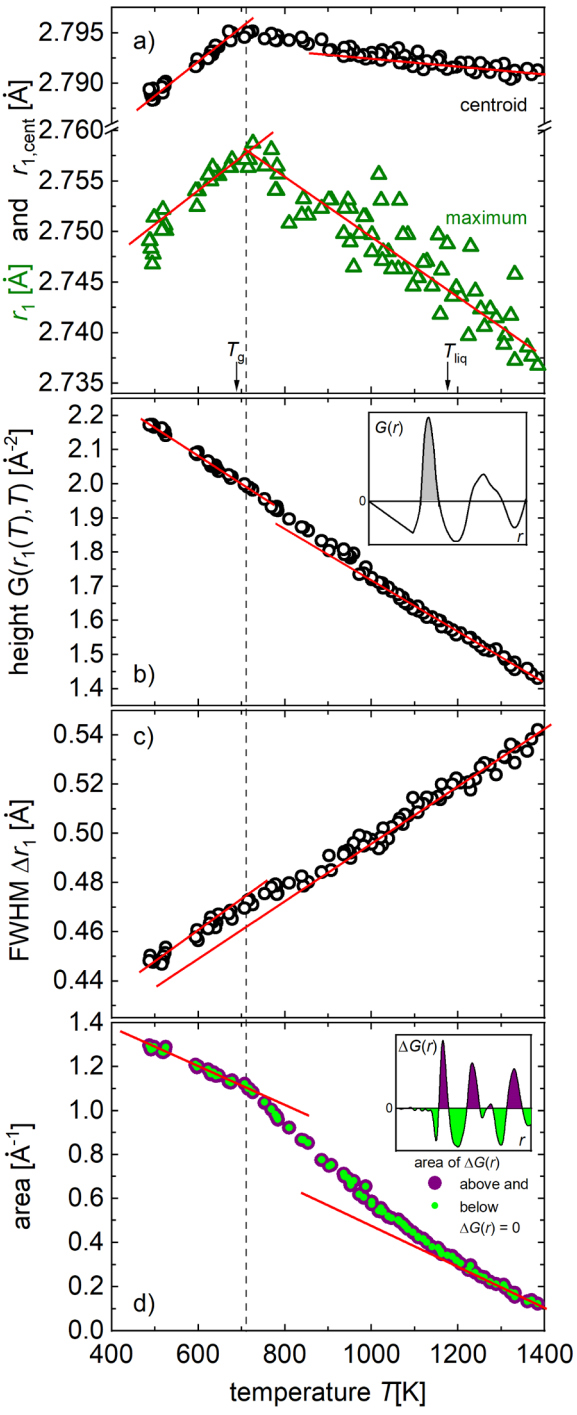

Fig. 5. Structural metrics of $Ti_{40}Zr_{10}Cu_{34}Pd_{14}Sn_2$ in real space during free cooling derived from the first peak (first shell, $n = 1$, relevant portion shaded in grey in the inset in b)) of the reduced pair distribution $G(r, T)$. a) position of the maximum $r_1(T)$ (green triangles) and the centroid $r_{1,\mathrm{cent}}(T)$ (black circles), b) the peak height $G(r_1(T), T)$, c) its full width at half maximum (FWHM) and d) the integrated area of $\Delta G(r, T)$ below and above the baseline $\Delta G(r, T) = 0$. Arrows and lines as in Fig. 3.

space (Fig. 3). Changes below T_g can be attributed to the Debye-Waller factor.

Fig. 5a,b,c shows metrics derived for the first shell obtained by analogy with the first halo in reciprocal space. Additionally to the position of the centroid $r_{1,cent}(T)$ (black circles in Fig. 5a), as in reciprocal space, also the positions $r_1(T)$ of its maximum (green triangles) to characterise the shell distances are shown. Both $r_{1,cent}(T)$ and $r_1(T)$ show an apparent negative thermal expansion in the liquid and undercooled liquid regions which will be discussed below. Below T_g, as expected, a positive thermal expansion can be observed. The height $G(r_1(T), T)$ and the FWHM $\Delta r_1(T)$ show a quasi-linear behaviour over the complete T-range. The metrics for the first shell in real space presented in Fig. 5a–c do not reflect the changes in behaviour during cooling (accelerated ordering) as clearly as in reciprocal space. This may partially be attributable to the bigger scatter of the data. On the other hand, the values for the integrated areas of $\Delta G(r, T)$ (Fig. 5d), representing combined effect of all shells of a wide range of distances, reflect the accelerated ordering below T_{liq} very well, which resembles the behaviour known from $Zr_{60}Cu_{30}Al_{10}$ [3].

4. Discussion

Various models have been proposed to describe the structure of metallic glasses since the 1960s, including Bernal's dense random packing model of hard spheres [36], Gaskell's stereochemically designed local structure units [37] as well as the efficient space filling scheme of solute-centred clusters by Miracle [38]. The influence of global interactions between the valence electrons and atoms of an alloy has also been shown to have an influence on structure formation in metallic glasses [39–42]. It is now widely accepted that the structure of metallic glasses is based on atomic clusters that give rise to SRO and MRO, while the long-range order of crystalline materials is absent. For many glassy alloys, specific local structural motifs have been identified by simulations and experiments [43–45], including the direct observation of interconnected atomic polyhedra by nano-beam electron diffraction [46]. The local atomic packing order as well as topological arrangements of clusters are important features that enable not only the description of the structure of metallic glasses but also provide insights about structure-property relationships. The formation of various local atomic clusters is controlled by both atomic size ratios and chemical bonding. It is also widely accepted that local icosahedral and icosahedral-like order prevails in many metallic-glass forming alloys [46–48]. On the other hand, the local order in metallic liquids is less pronounced than in the glassy state as shown in Fig. 2 and Fig. 4. Although the prevailing type of polyhedra in the local atomic structure of Ti-based BMGs has not been unambiguously established yet, the formation of quasicrystals with icosahedral symmetry has been reported for some Ti-based alloys [15,32,49]. According to the hard-sphere packing model, an atomic size ratio $R_{A/B} = r_A / r_B = 0.902$ (r_A and r_B being the radii of centre and first-neighbour-shell atoms, respectively) is required to form an ideal icosahedral cluster around a central atom [50]. In the case of $Ti_{40}Zr_{10}Cu_{34}Pd_{14}Sn_2$ $R_{Ti/Cu}$ and $R_{Cu/Ti}$ are 1.127 and 0.887, respectively [51]. Thus, around Ti or Cu, which are the most abundant elements in this quinary alloy, icosahedral packing might not be favourable. However, especially the atomic size ratio $R_{Ti/Zr}$ (0.899) and to a lesser extent $R_{Ti/Sn}$ (0.916) [51] are closer to the ideal value of 0.902 and therefore the additional elements Zr and Sn may facilitate the formation of local icosahedral-like symmetry in the cooling liquid. This could also be the reason underlying the high GFA of Ti-Zr-Cu-Pd-Sn-alloys as compared to other Ti-based alloys [15,32,49]. However, further exploration is necessary to verify the developing local symmetry during cooling. The increase of the atomic populations in the shells with decreasing temperature as inferred from Fig. 4a and b could be the result of i) the rearrangement of atoms previously located in anti-shell regions (local minima in Fig. 4a) into atomic clusters with local symmetry as the temperature decreases, ii) the reorganisation of atomic clusters existing at higher temperatures into clusters with higher packing density at lower temperatures or iii) a combination of both mechanisms. Recent results from molecular-dynamics simulations in Zr-based metallic-glass forming alloys support the idea that the population of atomic clusters with icosahedral local symmetry increases faster than other clusters as the liquid metal is cooled towards T_g [2,3,47].

With the exception of Cu-Sn (and Ti-Zr) all atomic pairs of $Ti_{40}Zr_{10}Cu_{34}Pd_{14}Sn_2$ have negative heats of mixing (Table 2) which supports good GFA according to one of the main (empirical) criteria suggested by Inoue [10].

In a simplistic approach, glass formation can be described as the rapid cooling of the amorphous structure of a liquid down to the glass transition temperature T_g below which it "freezes" to become an amorphous solid. However, below T_{liq}, crystalline phases are thermodynamically favoured and a remarkable slowdown of the kinetics in the undercooled liquid is necessary to suppress crystal nucleation and growth during solidification. This kinetic arrest is manifested by a significant increase of viscosity in the undercooled liquid whose origins remain only poorly understood [7,56].

To relate the evolution of the atomic structure to the evolution of the viscosity, Fig. 3a shows literature data [4] for $\eta(T)$ of the very similar Ti-based alloy $Ti_{40}Zr_{10}Cu_{30}Pd_{20}$ (T_g = 687 K [16] and T_{liq} = 1279 K [34]) as such data for $Ti_{40}Zr_{10}Cu_{34}Pd_{14}Sn_2$ itself were not available. The curved behaviour of e.g. $Q_{1,cent}(T)$ and $S(Q_1(T), T)$ is reflected, even though much more pronounced, by $\eta(T)$ which increases by ≈ 1.5 orders of magnitude in the small T-range for which data are available. This observation strongly supports the idea that the sharp increase of the viscosity, the kinetic arrest as well as the structural changes in the undercooled liquids may have the same origin [1–4]. The increasing slope observed in the structural metrics as function of T points to an acceleration of the atomic rearrangements during undercooling towards T_g (Fig. 3a). For Pd- and Zr-based BMG-forming alloys, direct structural signatures of the viscosity increase and, hence, fragility of the undercooled liquid could be identified [1,2]. In these materials, the peak in $G(r)$ representing the first shell can be decomposed into two sub-peaks by fitting Gaussian functions. The evolution of the ratio of the areas under these two functions during undercooling between T_{liq} and T_g strongly resembles the evolution of the viscosity in this temperature range. The change of this ratio has been associated with the change in activation energy during undercooling, providing a structural measure for fragility [1,2,57]. In the present case, the first peak of $G(r)$ cannot be unambiguously deconvolved into subpeaks. However, applied to the second shell, a similar behaviour can be observed (Fig. S3 in the Supplementary Material). Following the analysis used for $Pd_{40}Cu_{30}Ni_{10}P_{20}$ and $Zr_{55}Cu_{30}Ni_5Al_{10}$ [1,2,57], $Ti_{40}Zr_{10}Cu_{34}Pd_{14}Sn_2$ is found to be a

Table 2
Heats of mixing ΔH_{mix} (according to Miedema's model) [52], interatomic distances d_{at} [51], Faber-Ziman weights W_{ij} [53] and probabilities for random contact P_{ij} [54,55] for all atomic pairs i-j occurring in $Ti_{40}Zr_{10}Cu_{34}Pd_{14}Sn_2$.

pair i-j	ΔH_{mix} [kJ/mol]	d_{at} [Å]	W_{ij}	P_{ij}
Ti-Ti	0	2.84	0.085	0.160
Cu-Ti	−9	2.68	0.192	0.272
Cu-Cu	0	2.52	0.107	0.116
Pd-Ti	−65	2.84	0.125	0.112
Pd-Cu	−14	2.68	0.14	0.095
Pd-Pd	0	2.84	0.046	0.020
Zr-Ti	0	3	0.078	0.080
Zr-Cu	−23	2.84	0.087	0.068
Zr-Pd	−91	3	0.057	0.028
Zr-Zr	0	3.16	0.018	0.010
Sn-Ti	−21	2.97	0.019	0.016
Sn-Cu	7	2.81	0.022	0.014
Sn-Pd	−34	2.97	0.014	0.006
Sn-Zr	−43	3.13	0.009	0.004
Sn-Sn	0	3.1	0.001	0.001

comparatively strong liquid, in accord with viscosity measurements [4] (Section S3 of the Supplementary Material).

Upon further cooling, the kink occurring near the calorimetric glass transition temperature T_g indicates the "freezing" of the amorphous structure, i.e. structural changes have ceased to dominate and the linear change of $Q_{1,cent}(T)$ below T_g can mainly be attributed to usual thermal expansion only (Fig. 3a). The linear increase of $S(Q_1(T), T)$, with a much smaller slope, together with the almost constant $\Delta Q_1(T)$ below T_g indicate that the behaviour is now dominated by the Debye-Waller factor (Fig. 3b,c).

As mentioned above, an apparent negative thermal expansion can be observed for the first shell ($n = 1$) above T_g. This phenomenon has been reported before, and different possible explanations have been put forward [58–61]. Fig. 6 shows the positions of the centroids up to the eighth shell ($n = 8$) normalised to the respective value at 487 K. The use of centroids provides the possibility to obtain a measure for the distance also for shells with high n where a proper fit is hampered by termination ripples. The different behaviour of the first shell in comparison with all other shells can clearly be seen. Interestingly, for $n = 2$ and $n = 3$ the shell distances behave very similarly to each other, but show a much stronger thermal expansion than for $n > 3$. Except for $n = 7$ all other shells behave virtually alike within the experimental uncertainty. Hints for the existence of two structural regions with a demarcation between $n = 3$ and $n = 4$ were recently reported for glassy $Zr_{60}Cu_{20}(Cu,Ni,Co)_{10}Al_{10}$ alloys where a possible explanation was given in terms of the influence of the electronic structure [33]. The availability of T-dependent measurements in the present case enables a more detailed study of this behaviour. Also shown in Fig. 6 are $2\pi/Q_1(T)$ (solid red line on yellow background) and $2\pi/Q_{1,cent}(T)$ (dash-dotted red line on yellow background), respectively. A good agreement for $n \geq 4$ (again with the exception of $n = 7$) is obvious. These observations corroborate the early conjecture by Cargill [62] that the first maximum in $S(Q)$ represents the MRO (but not SRO) from a certain distance onwards [62,63]. The peculiar behaviour of shells 2 and 3, that seemingly can neither be assigned to SRO or MRO, needs further attention in the future. As for the different behaviour for $n = 7$ it is currently not clear whether this is a structural feature or merely an experimental artefact.

Since according to Yavari et al., the macroscopic thermal expansion is correlated with $Q_1(T)$ [31], the present results indicate that above T_g only the behaviour for relatively high distances of the MRO, but not that for smaller distances, especially not that for the SRO ($n = 1$), can be used to evaluate thermal expansion in real space. A similar behaviour was described for glassy $Cu_{65}Zr_{35}$ [64] and liquid and glassy

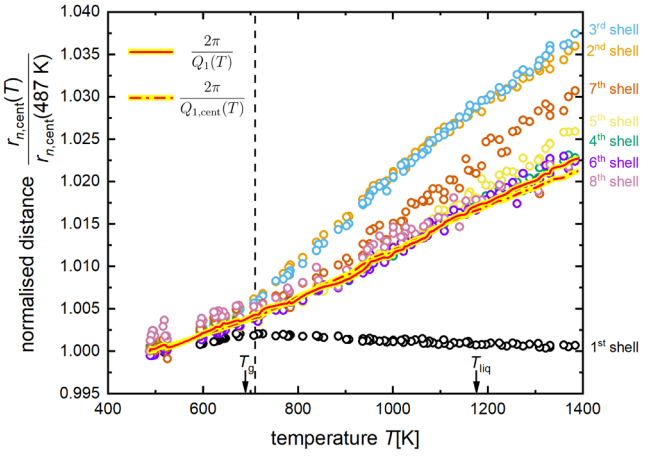

Fig. 6. Positions of the centroids of the first 8 shells normalised to their respective values at $T = 487$ K. Additionally, again normalised to their respective values at $T = 487$ K, $2\pi/Q_1(T)$ (solid red line on yellow background) and $2\pi/Q_{1,cent}(T)$ (dash-dotted red line on yellow background) are plotted for comparison. Arrows and vertical line as in Fig. 3.

$Pd_{40}Cu_{30}Ni_{10}P_{20}$ where T-dependent changes of the distances of the individual shells were compared to the macroscopic thermal expansion obtained by dilatometry [65]. Together with the present results, this suggests that the link between macroscopic thermal expansion and $Q_1(T)$, as stated by Yavari et al. [31], also holds for the undercooled liquid range. Below T_g no structural changes take place anymore and all shells behave roughly in the same way showing mainly the effects of thermal expansion (Fig. 6) corroborating the findings in reciprocal space discussed above. In general, it can be assumed that SRO and MRO are affected differently during undercooling towards vitrification. Structural changes beyond a usual linear thermal expansion manifest themselves mainly in the first three shells, highlighting again that this region should not be used to describe thermal expansion.

If the correlation between $Q_1(T)$ and the high-r part of $G(r)$ holds, changes in slope observed for the first halo in reciprocal space should also be visible in real space for the shell distances for higher n. Furthermore, due to the possibility of different effects on different length scales, changes in behaviour may occur at different characteristic temperatures for different shells. However, the scatter of the present data prevents a more detailed analysis.

It is interesting to note that the positions of the maxima $r_n(T)$ as well as those of their centroids $r_{n,cent}(T)$ for the peaks in $G(r, T)$ coincide with each other for $n \geq 4$ (Fig. S2 in the Supplementary Material), which indicates a transition of prevalence from local to global mechanisms of structure formation of the real space structure between $n = 3$ and $n = 4$: the influence of the individual local properties of the elemental species (i.e. mainly their radii) has ceased to dominate and is more and more replaced by a global statistical distribution (particle density oscillations [66,67]) irrespective of the particular element, underlining the above-mentioned reason for the demarcation put forward previously [33]. Indeed, Q_1 is also connected to a description of the structure of metallic glasses in terms of global interactions between atomic and electronic structure neglecting the differences between the individual species [40,41]. In this model the energetically optimal state for an alloy is reached when the "resonance condition" $Q_1 = 2k_F$ is fulfilled, i.e. the pseudo Brillouin-zone (diameter Q_1) coincides with the Fermi sphere (diameter $2k_F$) [39,40,68]. In this case a sequence of distances, known as spherical periodic order (SPO), for the consecutive shells from the central atom according to $r_n = (1/4 + n)\cdot 2\pi/Q_1$ is expected [40]. This relation would suggest a parallel behaviour of *all* shells depending only on Q_1, which, at least in the present case, is clearly contradicted by the results presented in Fig. 6. The global description, therefore, seems to be valid for the higher distances within the MRO only ($n \geq 4$) where the influence of local effects between the atoms is negligible as discussed above. In this respect a description of the real-space structure of metallic glasses based on global electronic interactions, especially by invoking the SPO, has to be reconsidered for small distances ($n \leq 3$). It is worth noting that a mean valence $Z \approx 1.5$ (electrons per atom), which has been discussed for other metallic glasses as well [41,69,70], seems to be an appropriate value to obtain a Fermi-sphere diameter $2k_F$ to be compatible with Q_1 or $Q_{1,cent}$, respectively, observed in the present case (cf. Supplementary Material for details of the related calculations).

In a sense, the measurement of the temperature-dependent shell distances $r_n(T)$, especially in the undercooled liquid region, acts as a powerful tool to probe the correlations between the different regions in real (SRO and MRO, respectively) and reciprocal space (halo 1) and helps to clarify the role of global effects in metallic glasses: shells for $n \leq 3$ seem to be strongly influenced by local effects which are also responsible for the apparent negative thermal expansion, whereas for $n \geq 4$ shells reflect global effects and are compatible with an expected positive (macroscopic) thermal expansion. Above T_g global electronic effects can influence the nature of the atomic arrangement in the MRO during undercooling. Below T_g, i.e. after structure formation has largely ceased, changes in shell distances take place foremost due to thermal expansion affecting all length scales almost identically. The different influence of global electronic effects on different length scales cannot be

discerned easily anymore, potentially leading to the false impression that they are equally as important in the SRO as well.

5. Conclusions

The evolution of the structure of $Ti_{40}Zr_{10}Cu_{34}Pd_{14}Sn_2$ metallic liquid during vitrification has been observed in-situ using high-energy synchrotron radiation and aerodynamic levitation. X-ray diffraction data have been recorded over a wide temperature range starting from above the liquidus temperature T_{liq} down to well below the glass-transition temperature T_g. The structural evolution has been analysed in terms of the temperature-dependent structure factor $S(Q, T)$ and reduced pair distribution function $G(r, T)$. Below T_{liq} rapid structural changes occur by atoms migrating from anti-shell to shell regions leading to a strong enhancement of the short and medium range order as T_g is approached. The structural rearrangements in the undercooled liquid of $Ti_{40}Zr_{10}Cu_{34}Pd_{14}Sn_2$ are found to be correlated with a rapid increase in viscosity and fragility. The structural rearrangements also cause an apparent negative thermal expansion of the first-nearest-neighbour shell in the undercooled liquid while in the glassy state a usual positive expansion occurs. Shells 2 and 3 cannot be clearly associated with either short or medium range order. The validity of a global description of the structure of metallic glasses, at least in the present alloy, is restricted to distances beyond the third shell. The results on the evolution of the atomic structure of metallic liquids during vitrification shed some more light on glass formation and on the structural origins of the sluggish long-range order kinetics that suppresses nucleation and growth of crystalline phases.

CRediT authorship contribution statement

Konstantinos Georgarakis: Conceptualisation, Methodology, Formal analysis, Validation, Writing - Original Draft, Visualisation, Project administration, Supervision, Funding acquisition. Martin E. Stiehler: Writing - Original Draft, Data Curation, Validation, Formal analysis, Methodology, Software, Visualisation. Louis Hennet: Methodology, Resources, Writing - Review & Editing, Validation, Data Curation. Yaofeng Guo: Formal analysis, Data Curation, Visualisation, Writing - Review & Editing. Jerzy Antonowicz: Conceptualisation, Methodology, Validation, Writing - Review & Editing. Dmitri V. Louzguine-Luzgin: Conceptualisation, Methodology, Validation, Writing - Review & Editing. Mark R. Jolly: Supervision, Writing - Review & Editing, Funding acquisition. Jérôme Andrieux: Methodology, Resources, Data Curation, Validation, Writing - Review & Editing. Gavin B.M. Vaughan: Methodology, Resources, Data Curation, Writing - Review & Editing. A. Lindsay Greer: Formal analysis, Validation, Writing - Review & Editing.

Declaration of Competing Interest

The authors declare the following financial interests/personal relationships which may be considered as potential competing interests: Martin E Stiehler reports financial support was provided by Engineering and Physical Sciences Research Council. Konstantinos Georgarakis reports financial support was provided by Engineering and Physical Sciences Research Council. Konstantinos Georgarakis reports financial support was provided by Japan Society for the Promotion of Science London. Konstantinos Georgarakis reports financial support was provided by European Commission Seventh Framework Programme for Research and Technological Development People. Yaofeng Guo reports financial support was provided by European Commission Seventh Framework Programme for Research and Technological Development People. If there are other authors, they declare that they have no known competing financial interests or personal relationships that could have appeared to influence the work reported in this paper

Acknowledgements

This work is dedicated to the memory of Professor AR Yavari. The authors extend gratitude to the ID15 beamline staff at the European Synchrotron Radiation Facility (ESRF) for their untired experimental support. Financial support by the ‘‘BioTiNet’’ EU Initial Training Network (ITN) (Grant agreement ID: 264635), the JSPS KAKENHI (Grant Number: 15K18201) as well as the EPSRC-DTP studentship “Bulk Metallic Glasses: Revealing the Structural Pathway of Liquid Metals to Vitrification” (project reference 2043971) within the framework of the EPSRC Doctoral Training Partnership with Cranfield University (EP/N509450/1) is gratefully acknowledged. MES thankfully acknowledges the support by a Cranfield University 75th Anniversary Research Fellowship.

Appendix A. Supporting information

Supplementary data associated with this article can be found in the online version at doi:10.1016/j.jallcom.2025.180214.

References

[1] D.V. Louzguine-Luzgin, R. Belosludov, A.R. Yavari, K. Georgarakis, G. Vaughan, Y. Kawazoe, T. Egami, A. Inoue, Structural basis for supercooled liquid fragility established by synchrotron-radiation method and computer simulation, J. Appl. Phys. 110 (2011) 043519, https://doi.org/10.1063/1.3624745.
[2] D.V. Louzguine-Luzgin, K. Georgarakis, J. Andrieux, L. Hennet, T. Morishita, K. Nishio, R.V. Belosludov, An atomistic study of the structural changes in a Zr-Cu-Ni-Al glass-forming liquid on vitrification monitored in-situ by X-ray diffraction and molecular dynamics simulation, Intermetallics 122 (2020) 106795, https://doi.org/10.1016/j.intermet.2020.106795.
[3] K. Georgarakis, L. Hennet, G.A. Evangelakis, J. Antonowicz, G.B. Bokas, V. Honkimaki, A. Bytchkov, M.W. Chen, A.R. Yavari, Probing the structure of a liquid metal during vitrification, Acta Mater. 87 (2015) 174–186, https://doi.org/10.1016/j.actamat.2015.01.005.
[4] N.A. Mauro, M. Blodgett, M.L. Johnson, A.J. Vogt, K.F. Kelton, A structural signature of liquid fragility, Nat. Commun. 5 (2014) 4616, https://doi.org/10.1038/ncomms5616.
[5] M. Stolpe, I. Jonas, S. Wei, Z. Evenson, W. Hembree, F. Yang, A. Meyer, R. Busch, Structural changes during a liquid-liquid transition in the deeply undercooled $Zr_{58.5}Cu_{15.6}Ni_{12.8}Al_{10.3}Nb_{2.8}$ bulk metallic glass forming melt, Phys. Rev. B. 93 (2016) 014201, https://doi.org/10.1103/PhysRevB.93.014201.
[6] C.A. Angell, The glass transition: an assessment of current thinking, Nucl. Phys. B (Proc. Suppl. 5 (1988) 69–80, https://doi.org/10.1016/0920-5632(88)90016-3.
[7] K. Ito, C.T. Moynihan, C.A. Angell, Thermodynamic determination of fragility in liquids and a fragile-to-strong liquid transition in water, Nature 398 (1999) 492–495, https://doi.org/10.1038/19042.
[8] L. Hennet, V. Cristiglio, J. Kozaily, I. Pozdnyakova, H.E. Fischer, A. Bytchkov, J.W. E. Drewitt, M. Leydier, D. Thiaudière, S. Gruner, S. Brassamin, D. Zanghi, G. J. Cuello, M. Koza, S. Magazù, G.N. Greaves, D.L. Price, Aerodynamic levitation and laser heating: applications at synchrotron and neutron sources, Eur. Phys. J. Spec. Top. 196 (2011) 151–165, https://doi.org/10.1140/epjst/e2011-01425-0.
[9] N.A. Mauro, K.F. Kelton, A highly modular beamline electrostatic levitation facility, optimized for in situ high-energy x-ray scattering studies of equilibrium and supercooled liquids, Rev. Sci. Instrum. 82 (2011), https://doi.org/10.1063/1.3554437.
[10] A. Inoue, Stabilization of metallic supercooled liquid and bulk amorphous alloys, Acta Mater. 48 (2000) 279–306, https://doi.org/10.1016/S1359-6454(99)00300-6.
[11] A.L. Greer, Metallic glasses…on the threshold, Mater. Today 12 (2009) 14–22, https://doi.org/10.1016/S1369-7021(09)70037-9.
[12] M. Chen, A brief overview of bulk metallic glasses, NPG Asia Mater. 3 (2011) 82–90, https://doi.org/10.1038/asiamat.2011.30.
[13] P.F. Gostin, O. Addison, A.P. Morrell, Y. Zhang, A.J.M.C. Cook, A. Liens, M. Stoica, K. Ignatyev, S.R. Street, J. Wu, Y.-L. Chiu, A.J. Davenport, In situ synchrotron X-ray diffraction characterization of corrosion products of a Ti-based metallic glass for implant applications, Adv. Healthc. Mater. 7 (2018) 1800338, https://doi.org/10.1002/adhm.201800338.
[14] M. Calin, A. Gebert, A.C. Ghinea, P.F. Gostin, S. Abdi, C. Mickel, J. Eckert, Designing biocompatible Ti-based metallic glasses for implant applications, Mater. Sci. Eng. C. 33 (2013) 875–883, https://doi.org/10.1016/j.msec.2012.11.015.
[15] Y. Guo, I. Bataev, K. Georgarakis, A.M. Jorge, R.P. Nogueira, M. Pons, A.R. Yavari, Ni- and Cu-free Ti-based metallic glasses with potential biomedical application, Intermetallics 63 (2015) 86–96, https://doi.org/10.1016/j.intermet.2015.04.004.
[16] S.L. Zhu, X.M. Wang, F.X. Qin, A. Inoue, A new Ti-based bulk glassy alloy with potential for biomedical application, Mater. Sci. Eng. A. 459 (2007) 233–237, https://doi.org/10.1016/j.msea.2007.01.044.
[17] E. Yüce, L. Zarazúa-Villalobos, B. Ter-Ovanessian, E. Sharifikolouei, Z. Najmi, F. Spieckermann, J. Eckert, B. Sarac, New-generation biocompatible Ti-based

metallic glass ribbons for flexible implants, Mater. Des. 223 (2022) 111139, https://doi.org/10.1016/j.matdes.2022.111139.
[18] A. Lachová, M. Stoica, Š. Michalik, P.F. Gostin, M. Fujioka-Kobayashi, B. Schaller, J.F. Löffler, P. Sovák, Modification of structural, mechanical, corrosion and biocompatibility properties of $Ti_{40}Zr_{10}Cu_{36}Pd_{14}$ metallic glass by minor Ga and Sn additions, J. Alloy. Compd. 940 (2023) 168776, https://doi.org/10.1016/j.jallcom.2023.168776.
[19] A. Rezvan, E. Sharifikolouei, V. Soprunyuk, W. Schranz, J. Todt, A. Lassnig, C. Gammer, N. August Sifferlinger, A. Asci, I. Okulov, S. Schlögl, J. Keckes, Z. Najmi, A. Cochis, A. Calogero Scalia, L. Rimondini, B. Sarac, J. Eckert, $Ti_{40}Zr_{10}Cu_{36}Pd_{14}$ bulk metallic glass as oral implant material, Mater. Des. 233 (2023) 112256, https://doi.org/10.1016/j.matdes.2023.112256.
[20] S.L. Zhu, X.M. Wang, A. Inoue, Glass-forming ability and mechanical properties of Ti-based bulk glassy alloys with large diameters of up to 1 cm, Intermetallics 16 (2008) 1031–1035, https://doi.org/10.1016/j.intermet.2008.05.006.
[21] N. Zheng, G. Wang, L.C. Zhang, M. Calin, M. Stoica, G. Vaughan, N. Mattern, J. Eckert, In situ high-energy x-ray diffraction observation of structural evolution in a Ti-based bulk metallic glass upon heating, J. Mater. Res. 25 (2010) 2271–2277, https://doi.org/10.1557/jmr.2010.0298.
[22] K. Kosiba, A. Rothkirch, J. Han, L. Deng, B. Escher, G. Wang, U. Kühn, J. Bednarcik, Phase formation of a biocompatible Ti-based alloy under kinetic constraints studied via in-situ high-energy X-ray diffraction, Prog. Nat. Sci. Mater. Int. 30 (2020) 432–436, https://doi.org/10.1016/j.pnsc.2020.06.004.
[23] J. Shen, Z. Lu, J.Q. Wang, S. Lan, F. Zhang, A. Hirata, M.W. Chen, X.L. Wang, P. Wen, Y.H. Sun, H.Y. Bai, W.H. Wang, Metallic glacial glass formation by a first-order liquid-liquid transition, J. Phys. Chem. Lett. 11 (2020) 6718–6723, https://doi.org/10.1021/acs.jpclett.0c01789.
[24] J. Shen, S.-L. Liu, Y. Sun, W. Wang, Metallic glacial glass, Natl. Sci. Open 2 (2023) 20220049, https://doi.org/10.1360/nso/20220049.
[25] M. Calin, M. Stoica, N. Zheng, X.R. Wang, S. Scudino, A. Gebert, J. Eckert, Thermal stability and crystallization kinetics of $Ti_{40}Zr_{10}Cu_{34}Pd_{14}Sn_2$ bulk metallic glass, Solid State Phenom. 188 (2012) 3–10, https://doi.org/10.4028/www.scientific.net/SSP.188.3.
[26] S.-I. Yamaura, S. Zhu, K. Abe, G. Xie, Ultrasonic fatigue of $Zr_{10}Cu_{34}Pd_{14}Sn_2$ glassy alloy, Open J. Met. 4 (2014) 56–64, https://doi.org/10.4236/ojmetal.2014.43007.
[27] D. Holland-Moritz, T. Schenk, P. Convert, T. Hansen, D.M. Herlach, Electromagnetic levitation apparatus for diffraction investigations on the short-range order of undercooled metallic melts, Meas. Sci. Technol. 16 (2005) 372–380, https://doi.org/10.1088/0957-0233/16/2/007.
[28] A.P. Hammersley, S.O. Svensson, M. Hanfland, A.N. Fitch, D. Hausermann, Two-dimensional detector software: from real detector to idealised image or two-theta scan, High. Press. Res. 14 (1996) 235–248, https://doi.org/10.1080/08957959608201408.
[29] P. Juhás, T. Davis, C.L. Farrow, S.J.L. Billinge, PDFgetX3: a rapid and highly automatable program for processing powder diffraction data into total scattering pair distribution functions, J. Appl. Crystallogr 46 (2013) 560–566, https://doi.org/10.1107/S0021889813005190.
[30] T. Egami, S.J.L. Billinge, Underneath the Bragg peaks: Structural Analysis of Complex Materials, Pergamon Press Ltd, 2003.
[31] A.R. Yavari, A.Le Moulec, A. Inoue, N. Nishiyama, N. Lupu, E. Matsubara, W. J. Botta, G. Vaughan, M.Di Michiel, Å. Kvick, Excess free volume in metallic glasses measured by X-ray diffraction, Acta Mater. 53 (2005) 1611–1619, https://doi.org/10.1016/j.actamat.2004.12.011.
[32] G.W. Lee, A.K. Gangopadhyay, R.W. Hyers, T.J. Rathz, J.R. Rogers, D.S. Robinson, A.I. Goldman, K.F. Kelton, Local structure of equilibrium and supercooled Ti-Zr-Ni liquids, Phys. Rev. B. 77 (2008) 184102, https://doi.org/10.1103/PhysRevB.77.184102.
[33] M.E. Stiehler, N.T. Panagiotopoulos, D.S. Keeble, Y.P. Ivanov, M. Menelaou, M. R. Jolly, A.L. Greer, K. Georgarakis, The effect of Ni or Co additions on the structure of $Zr_{60}Cu_{30}Al_{10}$ bulk metallic glass revealed by high-energy synchrotron radiation, Mater. Today Commun. 31 (2022) 103531, https://doi.org/10.1016/j.mtcomm.2022.103531.
[34] A.K. Gangopadhyay, M.E. Blodgett, M.L. Johnson, A.J. Vogt, N.A. Mauro, K. F. Kelton, Thermal expansion measurements by x-ray scattering and breakdown of Ehrenfest's relation in alloy liquids, Appl. Phys. Lett. 104 (2014) 191907, https://doi.org/10.1063/1.4876125.
[35] V.P. Voloshin, Y.I. Naberukhin, On the origin of the splitting of the second maximum in the radial distribution function of amorphous solids, J. Struct. Chem. 38 (1997) 62–70, https://doi.org/10.1007/BF02768808.
[36] J.D. Bernal, Geometry of the structure of monatomic liquids, Nature 185 (1960) 68–70, https://doi.org/10.1038/185068a0.
[37] P.H. Gaskell, A new structural model for transition metal-metalloid glasses, Nature 276 (1978) 484–485, https://doi.org/10.1038/276484a0.
[38] D.B. Miracle, A structural model for metallic glasses, Nat. Mater. 3 (2004) 697–702, https://doi.org/10.1038/nmat1219.
[39] S.R. Nagel, J. Tauc, Nearly-free-electron approach to the theory of metallic glass alloys, Phys. Rev. Lett. 35 (1975) 380–383, https://doi.org/10.1103/PhysRevLett.35.380.
[40] P. Häussler, Interrelations between atomic and electronic structures - liquid and amorphous metals as model systems, Phys. Rep. 222 (1992) 65–143, https://doi.org/10.1016/0370-1573(92)90018-U.
[41] M.E. Stiehler, M.R. Jolly, K. Georgarakis, On the impact of global interactions on the structure of metallic glasses, J. Alloy. Compd. 782 (2019) 496–505, https://doi.org/10.1016/j.jallcom.2018.12.086.
[42] C. Dong, Z.J. Wang, S. Zhang, Y.M. Wang, Review of structural models for the compositional interpretation of metallic glasses, Int. Mater. Rev. 0 (2019) 1–11, https://doi.org/10.1080/09506608.2019.1638581.
[43] H.W. Sheng, W.K. Luo, F.M. Alamgir, J.M. Bai, E. Ma, Atomic packing and short-to-medium-range order in metallic glasses, Nature 439 (2006) 419–425, https://doi.org/10.1038/nature04421.
[44] K. Georgarakis, A.R. Yavari, D.V. Louzguine-Luzgin, J. Antonowicz, M. Stoica, Y. Li, M. Satta, A. LeMoulec, G. Vaughan, A. Inoue, Atomic structure of Zr-Cu glassy alloys and detection of deviations from ideal solution behavior with Al addition by x-ray diffraction using synchrotron light in transmission, Appl. Phys. Lett. 94 (2009) 48–50, https://doi.org/10.1063/1.3136428.
[45] K. Georgarakis, A.R. Yavari, M. Aljerf, D.V. Louzguine-Luzgin, M. Stoica, G. Vaughan, A. Inoue, On the atomic structure of Zr-Ni and Zr-Ni-Al metallic glasses, J. Appl. Phys. 108 (2010) 1–7, https://doi.org/10.1063/1.3446131.
[46] A. Hirata, L.J. Kang, T. Fujita, B. Klumov, K. Matsue, M. Kotani, A.R. Yavari, M. W. Chen, Geometric frustration of icosahedron in metallic glasses, Science 341 (2013) 376–379, https://doi.org/10.1126/science.1232450.
[47] Y.Q. Cheng, E. Ma, H.W. Sheng, Alloying strongly influences the structure, dynamics, and glass forming ability of metallic supercooled liquids, Appl. Phys. Lett. 93 (2008) 111913, https://doi.org/10.1063/1.2987727.
[48] J. Antonowicz, A. Pietnoczka, W. Zalewski, R. Bacewicz, M. Stoica, K. Georgarakis, A.R. Yavari, Local atomic structure of Zr-Cu and Zr-Cu-Al amorphous alloys investigated by EXAFS method, J. Alloy. Compd. 509 (2011) S34–S37, https://doi.org/10.1016/j.jallcom.2010.10.105.
[49] Y.C. Kim, W.T. Kim, D.H. Kim, A development of Ti-based bulk metallic glass, Mater. Sci. Eng. A. 375–377 (2004) 127–135, https://doi.org/10.1016/j.msea.2003.10.115.
[50] D.B. Miracle, O.N. Senkov, A geometric model for atomic configurations in amorphous Al alloys, J. Non-Cryst. Solids 319 (2003) 174–191, https://doi.org/10.1016/S0022-3093(02)01917-8.
[51] D.B. Miracle, D.V. Louzguine-Luzgin, L.V. Louzguina-Luzgina, A. Inoue, An assessment of binary metallic glasses: correlations between structure, glass forming ability and stability, Int. Mater. Rev. 55 (2010) 218–256, https://doi.org/10.1179/095066010X12646898728200.
[52] A. Takeuchi, A. Inoue, Classification of bulk metallic glasses by atomic size difference, heat of mixing and period of constituent elements and its application to characterization of the main alloying element, Mater. Trans. Jim. 46 (2005) 2817–2829, https://doi.org/10.2320/matertrans.46.2817.
[53] T.E. Faber, J.M. Ziman, A theory of the electrical properties of liquid metals III. The resistivity of binary alloys, Philos. Mag. 11 (1965) 153–173, https://doi.org/10.1080/14786436508211931.
[54] C. Jelsch, K. Ejsmont, L. Huder, The enrichment ratio of atomic contacts in crystals, an indicator derived from the Hirshfeld surface analysis, IUCrJ 1 (2014) 119–128, https://doi.org/10.1107/S2052252514003327.
[55] X. Tong, G. Wang, Z.H. Stachurski, J. Bednarčík, N. Mattern, Q.J. Zhai, J. Eckert, Structural evolution and strength change of a metallic glass at different temperatures, Sci. Rep. 6 (2016) 30876, https://doi.org/10.1038/srep30876.
[56] C.A. Angell, K.L. Ngai, G.B. McKenna, P.F. McMillan, S.W. Martin, Relaxation in glassforming liquids and amorphous solids, J. Appl. Phys. 88 (2000) 3113–3157, https://doi.org/10.1063/1.1286035.
[57] D.V. Louzguine-Luzgin, Structural changes in metallic glass-forming liquids on cooling and subsequent vitrification in relationship with their properties, Materials 15 (2022) 7285, https://doi.org/10.3390/ma15207285.
[58] H. Lou, X. Wang, Q. Cao, D. Zhang, J. Zhang, T. Hu, H.-K. Mao, J.-Z. Jiang, Negative expansions of interatomic distances in metallic melts, Proc. Natl. Acad. Sci. 110 (2013) 10068–10072, https://doi.org/10.1073/pnas.1307967110.
[59] J. Ding, M. Xu, P.F. Guan, S.W. Deng, Y.Q. Cheng, E. Ma, Temperature effects on atomic pair distribution functions of melts, J. Chem. Phys. 140 (2014) 064501, https://doi.org/10.1063/1.4864106.
[60] J. Ding, E. Ma, Computational modeling sheds light on structural evolution in metallic glasses and supercooled liquids, Npj Comput. Mater. 3 (2017) 9, https://doi.org/10.1038/s41524-017-0007-1.
[61] A.K. Gangopadhyay, K.F. Kelton, A re-evaluation of thermal expansion measurements of metallic liquids and glasses from x-ray scattering experiments, J. Chem. Phys. 148 (2018) 204509, https://doi.org/10.1063/1.5032319.
[62] G.S. Cargill, Structure of metallic alloy glasses, in: H. Ehrenreich, F. Seitz, D. Turnbull (Eds.), Solid State Phys. - Adv. Res. Appl, Academic Press, 1975, pp. 227–320, https://doi.org/10.1016/S0081-1947(08)60337-9.
[63] D. Ma, A.D. Stoica, X.-L. Wang, Power-law scaling and fractal nature of medium-range order in metallic glasses, Nat. Mater. 8 (2009) 30–34, https://doi.org/10.1038/nmat2340.
[64] N. Mattern, J. Bednarcik, M. Stoica, J. Eckert, Temperature dependence of the short-range order of $Cu_{65}Zr_{35}$ metallic glass, Intermetallics 32 (2013) 51–56, https://doi.org/10.1016/j.intermet.2012.08.024.
[65] N. Mattern, H. Hermann, S. Roth, J. Sakowski, M.-P. Macht, P. Jovari, J. Jiang, Structural behavior of $Pd_{40}Cu_{30}Ni_{10}P_{20}$ bulk metallic glass below and above the glass transition, Appl. Phys. Lett. 82 (2003) 2589–2591, https://doi.org/10.1063/1.1567457.
[66] C.W. Ryu, T. Egami, Medium-range atomic correlation in simple liquids. I. Distinction from short-range order, Phys. Rev. E. 104 (2021) 064109, https://doi.org/10.1103/PhysRevE.104.064109.
[67] T. Egami, C.W. Ryu, World beyond the nearest neighbors, J. Phys. Condens. Matter Inst. Phys. J. 35 (2023), https://doi.org/10.1088/1361-648X/acbe24.

[68] H. Nowak, P. Häussler, Concept of resonances in disordered metallic matter, J. Non-Cryst. Solids 250 (1999) 389–392, https://doi.org/10.1016/S0022-3093(99)00269-0.

[69] S.S.A. Gillani, S. Schulze, P. Häussler, Scenarios of structure stabilization and their cooperations in $Al_{100-x}Mn_x$, J. Non-Cryst. Solids 447 (2016) 290–299, https://doi.org/10.1016/j.jnoncrysol.2016.04.037.

[70] Y.M. Wang, J.B. Qiang, C.H. Wong, C.H. Shek, C. Dong, Composition rule of bulk metallic glasses and quasicrystals using electron concentration criterion, J. Mater. Res. 18 (2003) 642–648, https://doi.org/10.1557/JMR.2003.0084.